



Switching on efficient photocatalytic water oxidation reactions over CaNbO₂N by Mg modifications under visible light illumination

Yawei Wang^{a,1}, Shu Jin^{b,1}, Xiaoqin Sun^a, Shunhang Wei^a, Long Chen^a, Xiaoxiang Xu^{a,*}

^a Shanghai Key Lab of Chemical Assessment and Sustainability, School of Chemical Science & Engineering, Tongji University, 1239 Siping Road, Shanghai, 200092, China

^b Clinical and Central Lab, Putuo People's Hospital, Tongji University, 1291 Jiangning Road, Shanghai, 200060, China



ARTICLE INFO

Keywords:

CaNbO₂N
Mg modification
Photocatalyst
Water splitting
Water oxidation

ABSTRACT

In spite of a strong visible light absorbance as far as 600 nm, CaNbO₂N generally exhibits poor photocatalytic activity under normal conditions because of various structural defects and poor charge mobility. In this work, we have synthesized a series of Mg-modified CaNbO₂N, i.e. CaNb_{1-x}Mg_xO_{2+y}N_{1-y} ($0 \leq x \leq 0.2$), and performed a detailed investigation on their crystal structures, optical absorption and other physicochemical properties. Our results show that there is a slight shrinkage of the unit cell and a blue-shift of absorption edges upon Mg incorporation into CaNbO₂N. The nitrogen contents as well as defects levels can be effectively tuned by altering the content of Mg. More strikingly, photocatalytic oxygen productions are much improved after Mg modifications under visible light irradiation ($\lambda \geq 420$ nm). An average oxygen production rate as much as ~ 126.8 umol h⁻¹ and an apparent quantum efficiency as high as $\sim 3.4\%$ at 420 ± 20 nm is achieved for CaNb_{0.9}Mg_{0.1}O_{2+y}N_{1-y} ($x = 0.1$). These improvements probably stem from a substantial decrease of Nb⁴⁺ defects in CaNbO₂N as well as slight positive shift of valence band maximum (VBM) after Mg modifications. Meanwhile, photoelectrochemical analysis suggests charge migration is somewhat enhanced in response to Mg modifications.

1. Introduction

With an aim to tackle the severe energy crisis and environmental degradation, great efforts have been devoted into search/development of clean and recyclable energy resources and technologies [1–6]. Photocatalytic water splitting into hydrogen and oxygen using particulate semiconductors has been studied extensively due to its technical simplicity as well as a promising scenario to build a clean and sustainable energy infrastructure using solar energy [7–10]. Notwithstanding these appealing prospects, conventional photocatalysts are subject to poor solar conversion efficiencies either due to deficient light absorption and/or rapid charge recombination phenomenon [11–14]. How to overcome these shortcomings so as to realize efficient water cleavage reactions on semiconductor photocatalyst remain real challenges. In particular, water oxidation half-reaction involves participation of four holes and four protons, being of energetic and mechanistic difficulty to cope with based on single semiconductor particle [15–18].

In these contexts, perovskite metal oxynitrides AM(O,N)₃ (A = La, Ca, Sr, Ba; M = Ti, Nb, Ta) have gained considerable attention not only because of their strong visible light absorption but also due to their

proper band edge positions that meet thermodynamic and overpotential needs of water splitting reactions [19–25]. Owing to these desirable properties, perovskite metal oxynitrides have been extensively investigated for potential applications in environmental remediation [26,27], CO₂ reduction [28–30], and water splitting [31–34]. Nevertheless, previous investigations on these materials suggest very poor photocatalytic activities for both water reduction and oxidation reactions, being highly incommensurate with their optical properties [35–37]. This has been attributed to various types of defects generated during sample preparation (high temperature in the presence of ammonia) that strongly promote electron-hole recombination and lower down crystal integrity [33,38–41]. Nevertheless, the structure of perovskite metal oxynitrides is highly flexible in terms of compositional modifications, therefore doping foreign element is a useful strategy to modify the perovskite metal oxynitrides and reduce the concentration of various defects [42,43]. For instance, Nb based perovskite oxynitrides such as ANb(O,N)₃ (A = La, Ca, Sr, Ba) is suffered by a high concentration of Nb⁴⁺ species that substantially degrade their photocatalytic performance [44–46]. Methods to remove or lower down the levels of Nb⁴⁺ species in these compounds seems to be critical to

* Corresponding author.

E-mail address: xxxu@tongji.edu.cn (X. Xu).

¹ Equal contributions.

achieving efficient photocatalytic activity. Previous studies suggest that compositional alteration by introducing alkaline (Li, Na, K, etc.) or alkaline earth (Mg, Ca) elements into metal oxynitrides serve as a useful way to boost photocatalytic activities [39,47–52]. As one of Nb-based perovskite-type oxynitride, CaNbO_2N with a band gap energy of 2.0 eV has been reported as the highest photocatalytic activity across the series ANb(O,N)_3 ($\text{A} = \text{La, Ca, Sr, Ba}$) [53,54]. Besides, the ionic radii of Mg^{2+} (65 pm) is very close to that of Nb^{5+} (70 pm), suggesting that Mg is a proper dopant for CaNbO_2N at B site. To the best of our knowledge, no previous work regarding the application of Mg-modified CaNbO_2N on the photocatalytic oxygen production has been reported.

Thereby, we take CaNbO_2N as an example and demonstrate a facile approach to realize efficient water oxidation reactions through Mg modifications i.e. $\text{CaNb}_{1-x}\text{Mg}_x\text{O}_{2+y}\text{N}_{1-y}$ ($0 \leq x \leq 0.2$) in this work. Our studies suggest that the photocatalytic activity of CaNbO_2N can be greatly enhanced by introducing Mg into B sites. In particular, apparent quantum efficiency (AQE) as high as 3.4% at 420 ± 20 nm has been achieved and stands as the highest AQE for CaNbO_2N reported to date. Further analysis reveals that such improvements probably arises from the reduction of Nb^{4+} defects and slight positive shift of valence band maximum (VBM) in response to Mg modifications. This simple strategy using alkaline earth cations as modifiers can be well extendable to other perovskite oxynitrides.

2. Experimental

2.1. Material synthesis

Mg-modified CaNbO_2N , i.e. $\text{CaNb}_{1-x}\text{Mg}_x\text{O}_{2+y}\text{N}_{1-y}$ ($0 \leq x \leq 0.2$), were synthesized via thermal ammonolysis of metal oxide precursors. The precursors were prepared by standard polymerized-complex (PC) method [49]. In a typical synthesis, 1.0000 g niobium pentachloride (NbCl_5 , Aladdin, 99.9 %) and 8.0000 g anhydrous citric acid (CA, Aladdin, 99.5%) were dissolved into 10 mL ethylene glycol (EG, Aladdin, GC grade) to form an Nb-citrate complex solution. Subsequently, 0.9712 g calcium nitrate tetrahydrate ($\text{Ca}(\text{NO}_3)_2 \cdot 4\text{H}_2\text{O}$, Aladdin, 99%) and 0.0882 g magnesium acetate tetrahydrate ($\text{Mg}(\text{CH}_3\text{COO})_2 \cdot 4\text{H}_2\text{O}$, Aladdin, 99%) were then added to the Nb-citrate complex solution. The mixed solution was kept at 200 °C on a heating plate with stirring until a transparent gel was formed and further heated to 300 °C for 3 h to promote polymerization. After a brown resin appeared, the resin was calcined in air at 650 °C for 5 h and 850 °C for another 5 h to remove organic residues. The resulting white precursors were transferred into a tube furnace and heated with a ramp rate of 5 °C min⁻¹ to 750 °C and kept for 5 h under flowing ultrapure NH₃ (flow rate: 300 mL min⁻¹, Jiaya Chemicals, 99.999 %). After cooling down naturally, the powders obtained were annealed at 300 °C for 5 h in air and then washed with dilute nitric acid for more than three times to remove residual ammonia. The resultant powders were dried in an oven at 80 °C for 12 h to obtain the catalysts powders. Pristine CaNbO_2N was prepared under the same conditions in the absence of Mg ($\text{CH}_3\text{COO})_2 \cdot 4\text{H}_2\text{O}$.

2.2. Materials characterization

X-ray powder diffraction (XRD) patterns of all products were recorded on a Bruker D8 Focus diffractometer (Bruker, Germany) to analyze crystal structure and phase purity. Cu K_{α1} radiation ($\lambda = 1.5405 \text{ \AA}$) and Cu K_{α2} ($\lambda = 1.5444 \text{ \AA}$) were applied as the incident radiations. Rietveld refinements on XRD data were performed by using the General Structure Analysis System (GSAS) software package [55]. Raman spectra were conducted by an inVia DXR Raman spectrometer (He-cd laser, wavelength 514 nm). UV-vis diffuse reflectance spectra were collected by UV-vis spectrophotometer (JASCO-750, Japan) equipped with an integrating sphere and analyzed using JASCO software suite. BaSO₄ powder was used as a reference non-absorbing

material. Microstructures of freshly prepared samples were examined using a field emission scanning electron microscope (FESEM, Hitachi S4800, Japan) and a transmission electron microscope (TEM, JEOL JEM-2100, Japan). Specific surface areas of freshly prepared samples were determined by NOVA 2200e adsorption instrument and were analyzed based on the Brunauer-Emmett-Teller (BET) model [56]. The nitrogen contents in all samples were obtained by thermogravimetric analysis (TGA) performed on Labsysevo system (SETRAM, France) with a heating rate of 10 °C min⁻¹ from room temperature up to 1200 °C in air atmosphere. Surface chemical compositions of as-prepared products and valence band scan were investigated using X-ray photoelectron spectroscopy (XPS, AXIS Ultra DLD) with a monochromatic Al K_α source. All XPS data were calibrated using the adventitious C 1s peak at 284.7 eV and fitted by XPSPEAKFIT software with Shirley backgrounds and Gaussian-Lorentzian function (Lorentzian weighting of 20%). The photoluminescence (PL) emission spectra of the products were performed using an Edinburgh FLS920 fluorescence spectrophotometer with 420 nm laser light source at room temperature.

2.3. Photocatalytic water oxidation

Photocatalytic water oxidation experiments were carried out in a top-irradiation-type glass reactor connected to a closed gas circulation and evacuation system (Perfect Light, LabSolar-IIAG). All sample powder were deposited with CoO_x cocatalyst by an impregnation method [57]. Sample powders were impregnated with aqueous Co (NO₃)₂ solution (0.01 M) under ultrasound bath and dried at 80 °C in air. The resultant powders were calcined under an NH₃ flow (250 mL min⁻¹) at 650 °C for 1 h and recalcined in air at 200 °C for another 1 h. The photocatalytic experiments were then conducted using 100 mg sample powders dispersed ultrasonically in 100 mL aqueous AgNO₃ solution (0.05 M) containing 0.2 g La₂O₃. AgNO₃ served as an electron scavenger to promote the water oxidation reactions and La₂O₃ was used to control the pH around 8.5. Visible light irradiation was generated by filtering the output of a 300 W Xeon lamp (Perfect Light, PLX-SXE300, China) using a UV cutoff filter ($\lambda \geq 420 \text{ nm}$). Monochromic light was produced by filtering the light beam using bandpass filter at 420 nm, 450 nm, 500 nm, 550 nm and 600 nm. The photon flux at individual wavelength was gauged by a quantum meter (Apogee MP-300). The gas produced in the reactor was analyzed by an on-line gas chromatograph (TECHCOMP, GC7900) with a thermal conductivity detector (5 Å molecular sieve columns and Ar carrier gas). The apparent quantum efficiency (AQE) was calculated from the following equation:

$$\text{AQE} = 4 \times \frac{\text{number of oxygen production per hour}}{\text{number of photon flux per hour}} \times 100\%$$

2.4. Photoelectrochemical (PEC) measurement

Photoelectrodes of freshly prepared samples were fabricated via the electrophoretic deposition (EPD) method [58,59]. Sample powders (40 mg) were dispersed in 40 mL acetone with 10 mg iodine (Sigma-Aldrich, ≥ 99.8%) under ultrasonication for 20 min. Two parallel FTO glasses (1 × 3 cm) were inserted into the suspension in parallel with a separation of 1 cm A constant bias of 20 V was applied between FTO glasses for 3 min to promote the deposition. The deposited FTO glasses were then calcined under N₂ at 400 °C for 1 h to remove absorbed iodine. 25 μL of TiCl₄ (Alfa-Aesar, 99.9%) methanol solution was dropped onto the glasses to minimize the exposure of naked FTO and was dried at 350 °C in air for 15 min. After repeating this procedure for six times, the glasses were heated under NH₃ flow (250 mL min⁻¹) at 350 °C for 1 h. The photoelectrochemical (PEC) measurements were conducted in a three-electrode model with Ag/AgCl electrode (in saturated KCl) and Pt foil (1 × 1 cm) as reference and counter electrodes, respectively. The electrolyte and buffer used for the PEC measurements is 0.1 M K₃Po₄

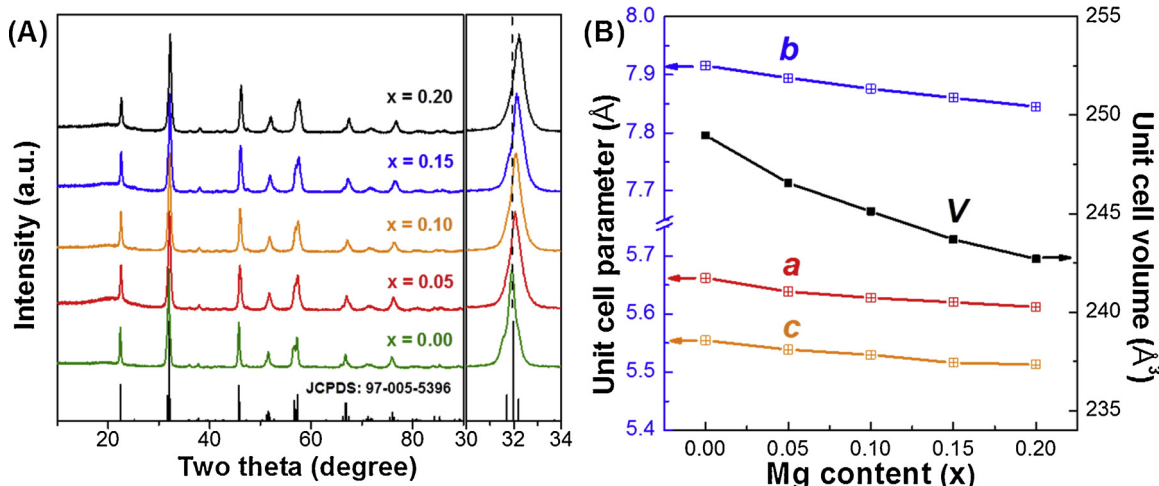


Fig. 1. (A) XRD patterns of freshly prepared samples $\text{CaNb}_{1-x}\text{Mg}_x\text{O}_{2+y}\text{N}_{1-y}$ ($0 \leq x \leq 0.2$) with different Mg levels, standard XRD patterns for CaNbO_2N (JCPDS: 97-005-5396) is also included; (B) unit cell parameters of individual sample with respect to Mg levels (x).

K_2HPO_4 aqueous solution at $\text{pH} = 7.95$. A 300 W Xenon lamp (Perfect Light, PLX-SXE300, China) equipped with UV cut-off filter ($\lambda \geq 420 \text{ nm}$) was used as a light source. Incident light illuminated on the photoelectrodes was rectified by an electronic timer and shutter (DAHENG, GCI-73, China).

3. Results and discussions

3.1. Crystal structure

The crystallographic structure and purity of freshly prepared products were examined by X-ray powder diffraction (XRD). As shown in Fig. 1A, the XRD patterns of all freshly prepared products exhibit similar profiles that can be indexed with an orthorhombic symmetry similar to that of pristine CaNbO_2N (JCPDS Card no. 97-005-5396) [60]. No impurity phase such as NbN or $\text{Ca}_2\text{Nb}_2\text{O}_7$ were detected, indicating single phase formation. Nevertheless, there is a clear shift of all diffraction peaks towards high angles after Mg modifications, suggesting shrinkage of CaNbO_2N unit cell in response to Mg uptake. This can be rationalized by the replacements of Nb^{5+} (ionic radius $\sim 70 \text{ pm}$) and N^{3-} (ionic radius $\sim 132 \text{ pm}$) with relatively small Mg^{2+} (ionic radius $\sim 65 \text{ pm}$) and O^{2-} (ionic radius $\sim 106 \text{ pm}$) in the CaNbO_2N perovskite lattice [48,61]. This is further supported by Rietveld refinements assuming that Mg and Nb, O and N are accommodated in the same crystallographic sites. Decrease of unit cell parameters that are associated with Mg incorporation can be clearly identified (Fig. 1B and Table 1). An illustration of refined XRD patterns and crystal structures of pristine CaNbO_2N and Mg modified one is displayed in Fig. 2. Shrinkage of unit cell normally results in shortening of bond length in the compound or in other words, increasing the bond strength. In our case, statistical average of $\text{Nb}-(\text{O},\text{N})$ bond before and after Mg modifications confirms this trend (Table 1). This is also verified by Raman

spectra that breathing mode of the $\text{Nb}(\text{O},\text{N})_6$ octahedron around 794 cm^{-1} are gradually shifted to larger wavenumber (Fig. 3), indicating stronger $\text{Nb}-(\text{O},\text{N})$ bond and mutual interactions between Nb and O/N [62,63]. Orbital overlapping between Nb 4d and O/N 2p is presumably increased due to closer placements of cations and anions and shall favor charge migrations. This is quite important as linkage of $\text{Nb}(\text{O},\text{N})_6$ octahedrons is severely distorted in CaNbO_2N , being disadvantageous for rapid charge transports [64,65].

3.2. UV-vis spectra

The color of as-prepared sample powders changes substantially upon Mg modifications. Pristine CaNbO_2N ($x = 0$) has a brownish color which turns gradually into yellow when the level of Mg increases from $x = 0.0$ to $x = 0.2$, as can be seen from the digital photograph in Fig. 4c. This is confirmed by the UV-vis diffuse reflectance spectra (DRS, Fig. 4a). The absorption edge of pristine CaNbO_2N approaches as far as 600 nm but is blue-shifted gradually after Mg modifications, indicating enlargement of band gap values. It is worth noting that the high absorption tail above 600 nm in case of pristine CaNbO_2N is effectively quenched in response to Mg modifications. Such an absorption tail is generally linked to various types of defects that often play negative roles during photocatalytic reactions. Thereby, introducing Mg into B site of CaNbO_2N appears to be quite useful to control these defect concentrations. The band gap values of individual samples are then determined by Kubelka-Munk transformation (Fig. 4b) and are tabulated in Table 2. Pristine CaNbO_2N owns a band gap of 2.05 eV which is consistent with the one reported [54]. Mg modifications slightly enlarge the band gap to 2.25 eV when x increases to 0.2, i.e. $\text{CaNb}_{0.8}\text{Mg}_{0.2}\text{O}_{2+y}\text{N}_{1-y}$.

3.3. Microstructure and thermogravimetric analysis

All freshly prepared samples were then examined by field emission scanning electron microscopy (FESEM) and transmission electron microscopy (TEM). As can be seen from Fig. 5 and Figure S1, all samples are composed of particles with size from 20 to 150 nm, which are considerably smaller than those prepared directly by solid state reactions [37,40]. This observation is typical for perovskite oxynitrides prepared using precursors from a PC method [25,50]. Decrease of particle size is beneficial for photocatalytic performance, not only because of a short charge migration pathway for charge migration from bulk to surface but also because of large surface areas hence more reaction sites. The specific surface areas were further determined by BET

Table 1

Unit cell parameters of freshly prepared samples $\text{CaNb}_{1-x}\text{Mg}_x\text{O}_{2+y}\text{N}_{1-y}$ ($0 \leq x \leq 0.2$), standard deviation is included in the parenthesis.

| x | S.G. | a (Å) | b (Å) | c (Å) | B.D. (Å) | V (Å ³) |
|------|------|-----------|-----------|-----------|-----------|---------------------|
| 0.00 | Pnma | 5.6621(3) | 7.9157(4) | 5.5547(3) | 2.0346(3) | 248.96(2) |
| 0.05 | Pnma | 5.6389(5) | 7.8944(8) | 5.5385(5) | 2.0325(1) | 246.55(4) |
| 0.10 | Pnma | 5.6280(3) | 7.8759(5) | 5.5296(3) | 2.0306(5) | 245.10(2) |
| 0.15 | Pnma | 5.6204(3) | 7.8559(5) | 5.5160(3) | 2.0281(2) | 243.68(3) |
| 0.20 | Pnma | 5.6120(4) | 7.8447(6) | 5.5128(4) | 2.0266(5) | 242.70(3) |

S.G.: space group; B.D.: average bond distance of Nb-O/N; V: volume of unit cell.

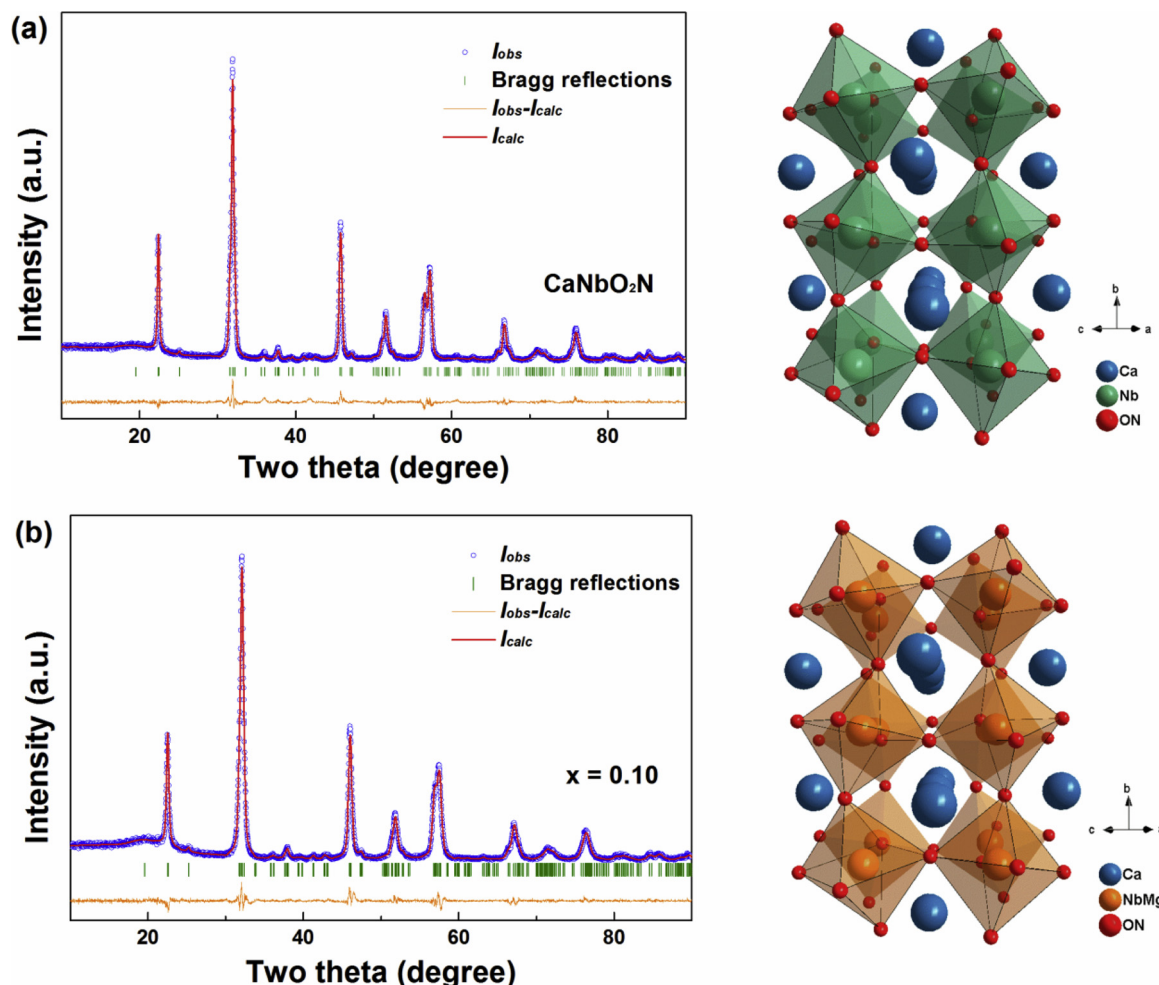


Fig. 2. Observed and calculated X-ray powder diffraction patterns of (a) pristine CaNbO_2N with good R -factors and χ^2 ($R_{\text{wp}} = 5.96\%$, $R_p = 5.08\%$, and $\chi^2 = 1.899$); (b) $\text{CaNb}_{1-x}\text{Mg}_x\text{O}_{2+y}\text{N}_{1-y}$ with good R -factors and χ^2 ($R_{\text{wp}} = 6.45\%$, $R_p = 5.36\%$, and reduced $\chi^2 = 1.483$), I_{obs} is observed diffraction data and I_{calc} is calculated data by the refinement. Refined crystal structures are illustrated at the right side.

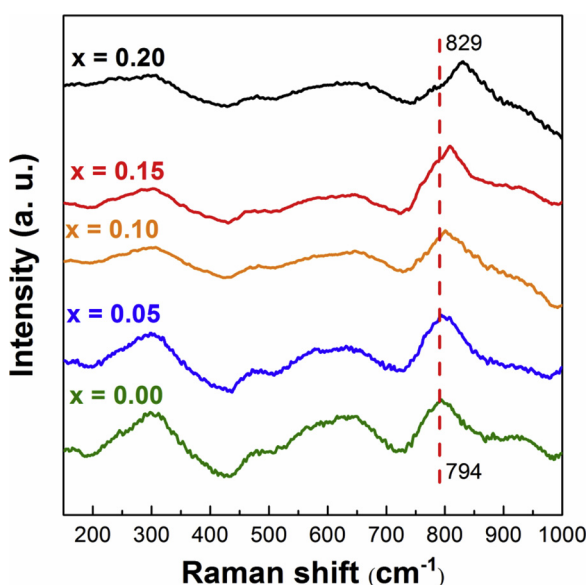


Fig. 3. Raman spectra of $\text{CaNb}_{1-x}\text{Mg}_x\text{O}_{2+y}\text{N}_{1-y}$ ($0 \leq x \leq 0.2$).

analysis. Nitrogen adsorption-desorption isotherms and pore-size distribution curves of all samples are illustrated in Figure S2. All isotherms exhibit type-II curves according to IUPAC classification, and all specific surface areas are listed in Table 2. High-resolution TEM images of pristine and Mg-modified CaNbO_2N are displayed in Fig. 6. The observed lattice fringes of (101) planes have a shrink from 3.94 \AA to 3.91 \AA after Mg incorporation, being consistent with XRD analysis. Thermogravimetric analysis (TGA) on as-prepared sample powders were performed in air at a temperature range from $20\text{ }^\circ\text{C}$ to $1200\text{ }^\circ\text{C}$ with a heating rate of $10\text{ }^\circ\text{C min}^{-1}$. Roughly three regions can be identified in all TGA curves (Fig. S3). First region corresponds to $20\text{ }^\circ\text{C}$ to $\sim 350\text{ }^\circ\text{C}$ where two successive mass losses can be seen [62]. These can be attributed to desorption of surface moistures. The second region lies between $\sim 350\text{ }^\circ\text{C}$ to $\sim 600\text{ }^\circ\text{C}$ and apparent increase of mass can be identified. This mass increase is ascribed to oxidation of perovskite oxynitride whereby oxygen is absorbed into the structure [54,66]. Further increase the temperature leads to gradual decrease of sample mass and therein lies the third region. This region has been frequently seen in various types of metal oxynitrides and is originated from the release of nitrogen species in the samples [67,68]. Deducting the influence of mass decrease tendency induced by crystal water and absorbed nitrogen, the nitrogen content in the prepared photocatalysts can be evaluated by assuming that the increase in mass was led by replacement of N with O during combustion process as following formula:

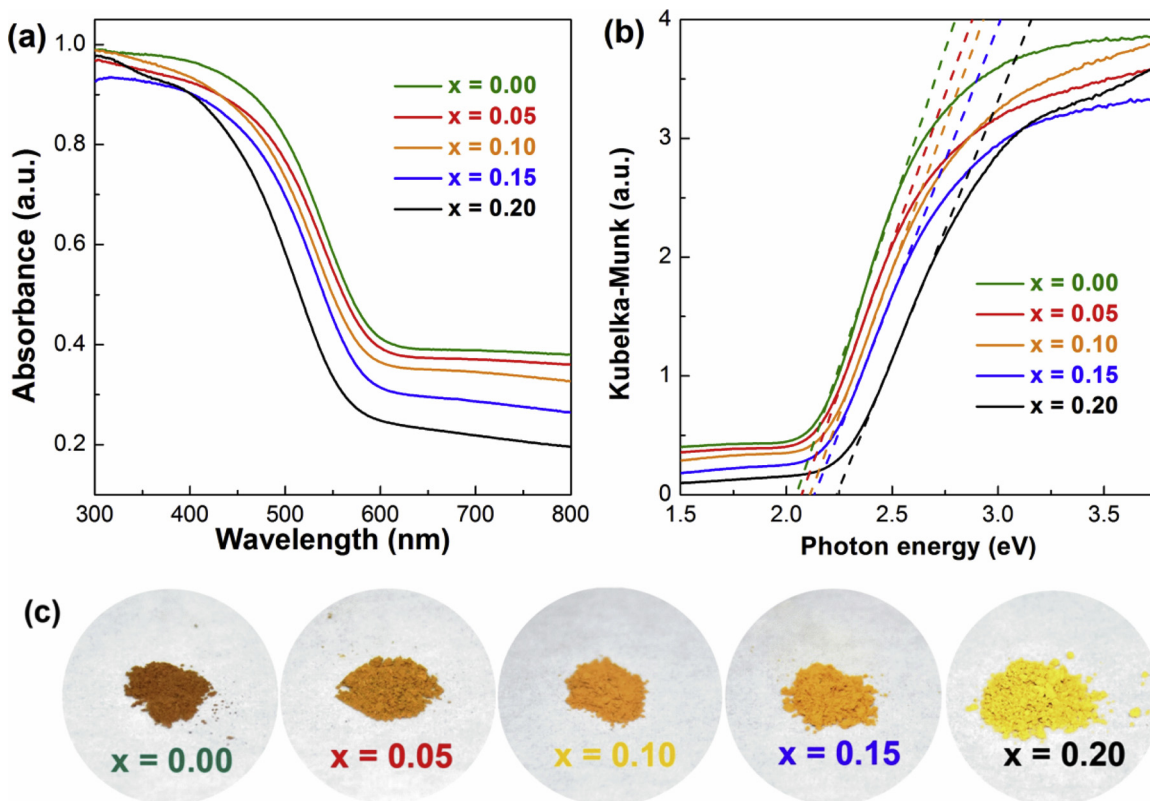
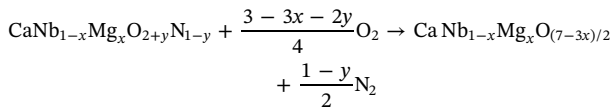


Fig. 4. (a) UV-vis light absorption spectra (converted from diffuse-reflectance spectra) of $\text{CaNb}_{1-x}\text{Mg}_x\text{O}_{2+y}\text{N}_{1-y}$ ($0 \leq x \leq 0.2$), (b) Kubelka-Munk transformation of the diffuse-reflectance data, (c) digital photograph of all as-prepared sample powders for visual inspections.



Obviously, Mg modifications clearly decrease the mass differences between the end of first and third region in the TGA curves. Thus, nitrogen contents (as tabulated in Table 2) within individual sample gradually decrease with Mg addition.

3.4. X-ray photoelectron spectra

Surface conditions of freshly prepared samples were investigated by XPS techniques. All energy scales were corrected by referencing to the adventitious C 1s peak centered at 284.7 eV. Fig. 7 shows the Nd 3d, O 1s, and Mg 1s high-resolution spectra of all samples. The Nb 3d state involves four overlapping peaks centered at 207.2 eV, 205.8 eV, 208.3 eV and 210.0 eV. Thereby, there are two types of Nb states in these samples. The peaks at low energy side, i.e. 205.8 eV and 208.3 eV, is assignable to Nb^{4+} species while those at high energy side, i.e. 207.2 eV and 210.0 eV typically belongs to Nb^{5+} species [7,69–71]. It is clear from the spectra that the peaks for Nb^{4+} species decrease appreciably after Mg modifications. The signals for O 1s state can be

identified as two overlapping peaks centered at 530.7 and 532.8 eV, being attributable to lattice oxygen (O^{2-}) and surface OH groups. Mg modifications generally increase the signal for OH groups thereby enhance the surface hydrophilicity [72]. The presence of Mg is also confirmed by a single peak centered at 1304.4 eV. The intensity of the peak is consistent with the increase of Mg levels within the samples. The Ca 2p and N 1s high-resolution spectra of all samples are displayed in Figure S4.

3.5. Photocatalytic oxygen production

Photocatalytic water oxidation of all sample powders was carried out by monitoring oxygen production in the presence of sacrificial agent under visible light illumination ($\lambda \geq 420$ nm). AgNO_3 was applied as an electron scavenger and CoO_x was employed as cocatalyst to promote water oxidation reactions [57,73]. All sample powders are able to produce oxygen continuously under visible light illumination, indicating that they are active photocatalysts for water oxidation reactions. However, slight Mg modifications ($x = 0.05$ and 0.1) clearly favor a higher oxygen production rate than pristine CaNbO_2N despite the fact that Mg modifications reduce visible light absorption. In particular, $\text{CaNb}_{0.9}\text{Mg}_{0.1}\text{O}_{2+y}\text{N}_{1-y}$ ($x = 0.1$) produces almost twice as

Table 2

Band gap values calculated from Kubelka-Munk transformations, effective chemical formula determined from TGA, BET specific surface area, pores volume and average pore size of as-prepared samples.

| x | Band gap (eV) | Effective chemical formula | BET surface area (m^2g^{-1}) | Pore volume (cm^3g^{-1}) | Average pore size (nm) |
|------|---------------|--|--|--|------------------------|
| 0.00 | 2.04(7) | $\text{CaNb}_{0.12}\text{N}_{0.88}$ | 6.74 | 0.134 | 5.6 |
| 0.05 | 2.10(4) | $\text{CaNb}_{0.95}\text{Mg}_{0.05}\text{O}_{2.27}\text{N}_{0.73}$ | 7.16 | 0.181 | 6.4 |
| 0.10 | 2.11(3) | $\text{CaNb}_{0.9}\text{Mg}_{0.1}\text{O}_{2.33}\text{N}_{0.67}$ | 7.54 | 0.213 | 7.2 |
| 0.15 | 2.15(2) | $\text{CaNb}_{0.85}\text{Mg}_{0.15}\text{O}_{2.63}\text{N}_{0.37}$ | 7.36 | 0.218 | 7.3 |
| 0.20 | 2.25(7) | - | 7.69 | 0.229 | 7.5 |

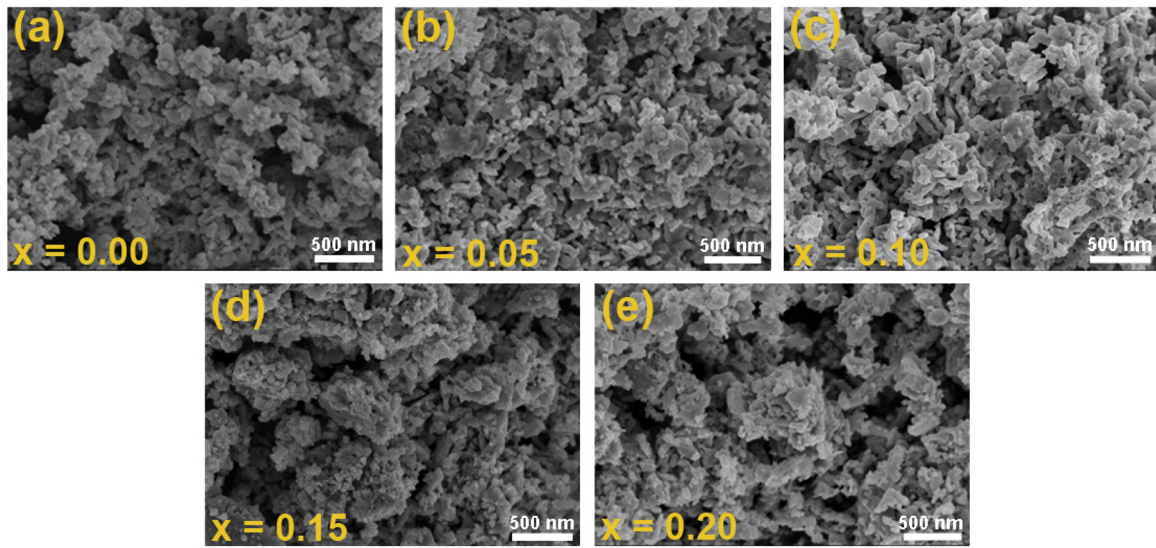


Fig. 5. Field emission scanning electron microscopy images of as-prepared samples $\text{CaNb}_{1-x}\text{Mg}_x\text{O}_{2+y}\text{N}_{1-y}$ ($0 \leq x \leq 0.2$): (a) $x = 0.00$; (b) $x = 0.05$; (c) $x = 0.10$; (d) $x = 0.15$ and (e) $x = 0.20$.

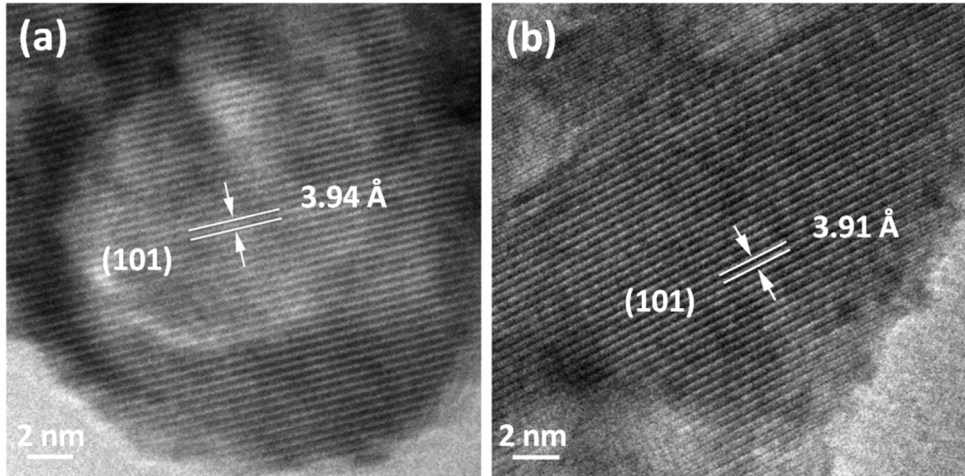


Fig. 6. High-resolution transmission electron microscopy images of (a) pristine CaNbO_2N and (b) $\text{CaNb}_{0.9}\text{Mg}_{0.1}\text{O}_{2+y}\text{N}_{1-y}$ ($x = 0.10$), respectively.

much oxygen as pristine CaNbO_2N for the whole experimental period (5 h), indicating the high efficiency of Mg as a modifier. Nevertheless, further increase the level of Mg results in a quick decrease of oxygen production rate. This is probably due to further reduction of visible light absorbance that counteracts positive effects of Mg modifications. A plot of oxygen production rate for the first hour is illustrated in

Fig. 8b. The rate is maximized at $x = 0.1$ which is more than two fold higher than pristine CaNbO_2N . The gradual decrease of oxygen production rate after the first hour illumination has been noticed for many systems using AgNO_3 as an electron scavenger and is attributed to the coverage of sample surface with metallic silver that blocks both light penetration and active reaction sites [74]. In Figure S5, XRD patterns of

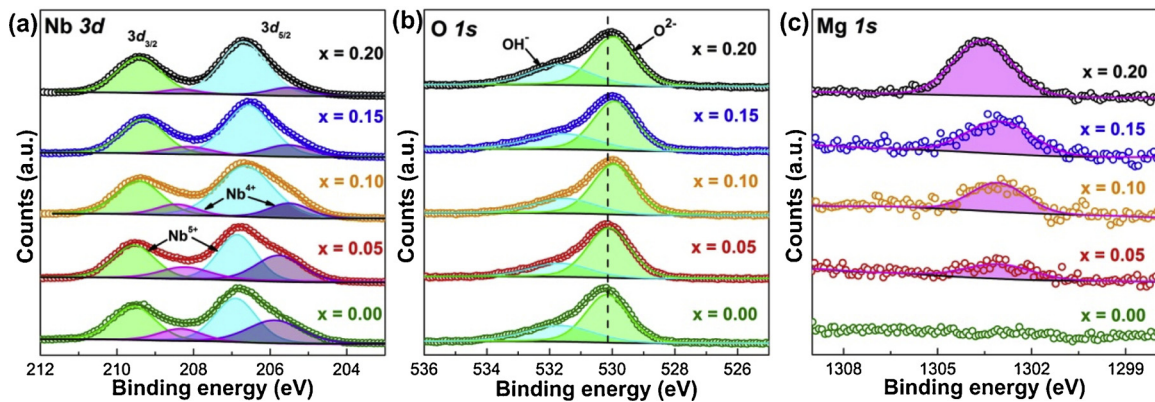


Fig. 7. XPS spectra of constituent elements of as-prepared samples: (a) Nb 3d; (b) O 1s; and (c) Mg 1s.

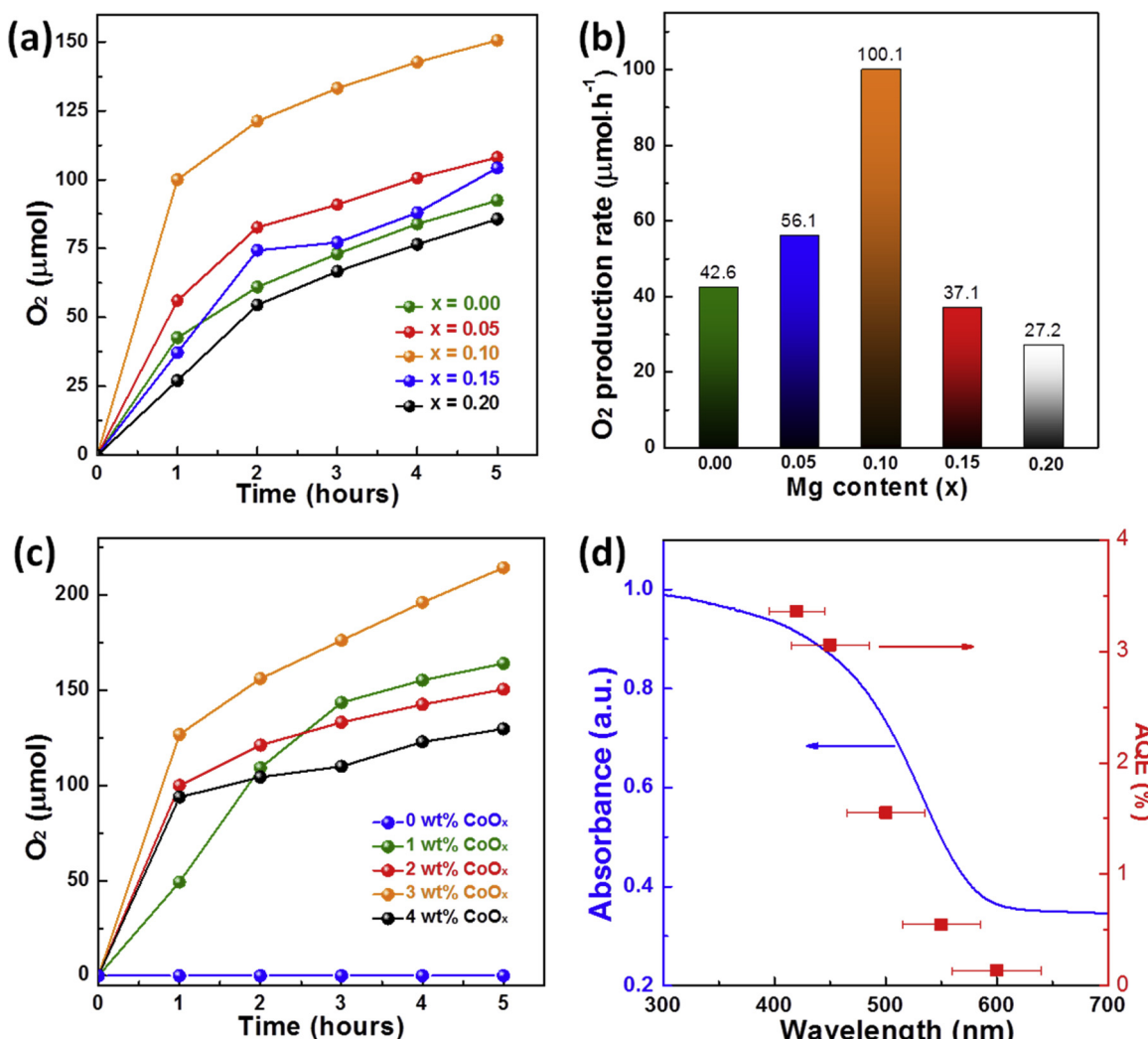


Fig. 8. (a) Photocatalytic oxygen evolution of as-prepared samples loaded with 2 wt% CoO_x under visible light irradiation ($\lambda \geq 420 \text{ nm}$); (b) first hour photocatalytic oxygen production rate for all samples; (c) photocatalytic oxygen evolution of $\text{CaNb}_{0.9}\text{Mg}_{0.1}\text{O}_{2+y}\text{N}_{1-y}$ ($x = 0.10$) loaded with different amounts of CoO_x ; (d) action spectrum of $\text{CaNb}_{0.9}\text{Mg}_{0.1}\text{O}_{2+y}\text{N}_{1-y}$ loaded with 3 wt% CoO_x .

$\text{CaNb}_{0.9}\text{Mg}_{0.1}\text{O}_{2+y}\text{N}_{1-y}$ ($x = 0.1$) shows the peaks of metallic silver after photocatalytic water oxidation reaction. In addition, the UV-vis light absorption spectra (Figure S6) of $\text{CaNb}_{0.9}\text{Mg}_{0.1}\text{O}_{2+y}\text{N}_{1-y}$ ($x = 0.1$) after photocatalytic reaction shows the obvious absorption tail above 600 nm, which is associated with metallic silver covered on the surface. The performance of Mg modified CaNbO_2N ($\text{CaNb}_{0.9}\text{Mg}_{0.1}\text{O}_{2+y}\text{N}_{1-y}$ ($x = 0.1$)) was further optimized by varying the amounts of cocatalyst loaded. A further 30% enhancement in oxygen production was achieved by increasing the CoO_x loading from 1 wt% to 3 wt% (Fig. 8c). The action spectra at 3 wt% CoO_x loading were then collected under monochromatic light illumination. The apparent quantum efficiency (AQE) agrees well with the absorption curve of $\text{CaNb}_{0.9}\text{Mg}_{0.1}\text{O}_{2+y}\text{N}_{1-y}$ ($x = 0.1$), confirming real photocatalytic processes. The AQE approaches as high as $3.4\% \pm 20 \text{ nm}$ which stands as the highest AQE reported on CaNbO_2N . The photocatalytic oxygen production and quantum efficiency of $\text{CaNb}_{0.9}\text{Mg}_{0.1}\text{O}_{2+y}\text{N}_{1-y}$ ($x = 0.1$) produced under optimized conditions are compared with other materials reported for photocatalytic oxygen production, such as pristine CaNbO_2N , CaTaO_2N , LaTaON_2 , LaNbON_2 and other metal oxynitrides, $\text{CaNb}_{0.9}\text{Mg}_{0.1}\text{O}_{2+y}\text{N}_{1-y}$ ($x = 0.1$) clearly outperforms these compound under the same conditions [36,37,45,53,54,75]. In addition, the cycling stability of $\text{CaNb}_{0.9}\text{Mg}_{0.1}\text{O}_{2+y}\text{N}_{1-y}$ ($x = 0.1$) is also measured by producing O_2 under visible light irradiation ($\lambda \geq 420 \text{ nm}$) Figure S7. The gradual

decrease of activity is due to the metallic silver deposited at the sample surface and a simple treatment with concentrated nitric acid clearly recovers the activity.

3.6. Photoelectrochemical investigations

To understand the origin of improved photocatalytic performance after Mg modifications, we then performed photoelectrochemical analysis on pristine and Mg-modified CaNbO_2N . Firstly, linear sweep voltammetry (LSV) was carried out on photoelectrodes fabricated using sample powders under chopped visible light illumination ($\lambda \geq 420 \text{ nm}$). Fig. 9a illustrates the typical LSV curves for pristine CaNbO_2N and $\text{CaNb}_{0.9}\text{Mg}_{0.1}\text{O}_{2+y}\text{N}_{1-y}$ ($x = 0.1$). Both samples exhibit anodic photocurrent under positive bias, indicative of n-type semiconductivity. However, Mg-modified CaNbO_2N exhibits a much higher photocurrent than pristine CaNbO_2N under the same conditions which agree well with the photocatalytic experiments. Considering the higher visible light absorption of pristine CaNbO_2N than $\text{CaNb}_{0.9}\text{Mg}_{0.1}\text{O}_{2+y}\text{N}_{1-y}$ ($x = 0.1$), severe charge recombination events are expected within pristine CaNbO_2N . Electrochemical impedance spectroscopy (EIS) was then conducted under both dark and light illumination conditions. Fig. 9b displays the Nyquist plot of impedance data measured frequency range from 100 kHz to 0.01 Hz. In both cases, Mg modified CaNbO_2N

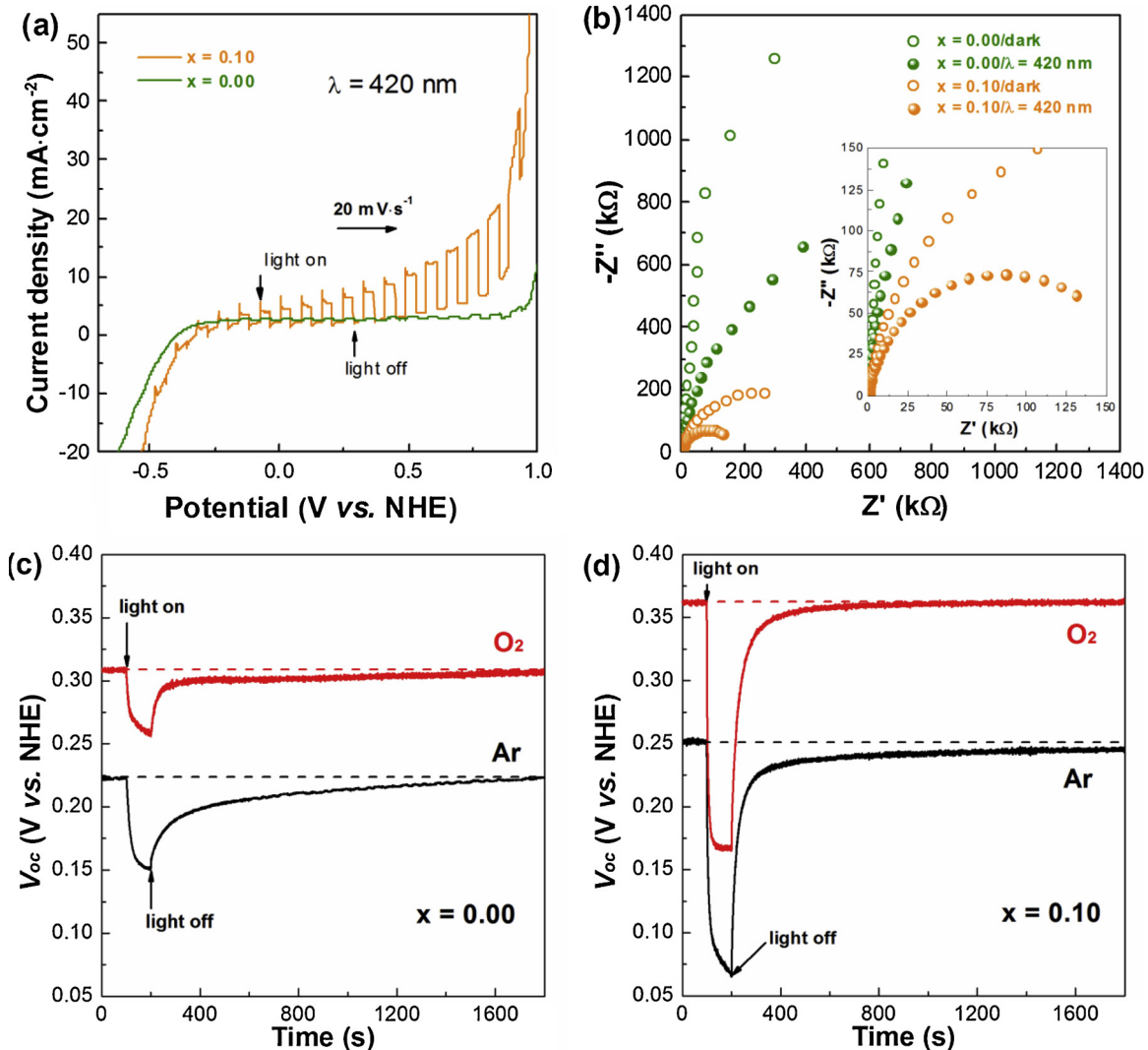


Fig. 9. (a) Linear sweep voltammetry (LSV) of the pristine and Mg-modified CaNbO₂N under chopped visible light irradiation ($\lambda \geq 420$ nm). The measurements were performed by sweeping the potential from -1.00 to 1.00 V_{NHE} at a scan rate of 20 mV s^{-1} in aqueous solution of K₃PO₄/K₂HPO₄ (0.1 M, pH = 7.95); (b) Nyquist plot of pristine and Mg-modified CaNbO₂N at open-circuit conditions under dark and visible light illumination ($\lambda \geq 420$ nm) conditions. Impedance was taken at frequency range from 10^5 to 10^{-2} Hz at 10 mV amplitude; V_{oc} time profile of (c) pristine and (d) Mg-modified CaNbO₂N under Ar and O₂, light illumination ($\lambda \geq 420$ nm) started after a stable V_{oc} in the dark was achieved and was terminated after 100 s.

exhibit a much smaller interfacial resistance than pristine CaNbO₂N, confirming a facile charge transfer at the semiconductor/electrolyte interface after Mg modifications. Furthermore, open-circuit voltage (V_{oc}) decay (OCVD) experiments were performed to investigate charge recombination events or electron dissipation pathways under both visible light illumination and dark conditions [76,77]. The experiments were conducted in different atmospheres, i.e. O₂ and Ar, in order to evaluate charge migration conditions within these samples. This is based on the fact that O₂ serves as an efficient electron scavenger as long as photo-generated electrons migrate to the sample surface [76]. Typical OCVD curves of pristine CaNbO₂N and CaNb_{0.9}Mg_{0.1}O_{2+y}N_{1-y} ($x = 0.1$) are illustrated in Fig. 9c and d. Both samples display a negative shift of V_{oc} upon light illumination, confirming again their n-type semiconductivity. After light termination in Ar atmosphere, V_{oc} decay profile of pristine CaNbO₂N took almost 1600 s for restoration back to dark value, suggesting a long lifetime of electrons. However, even longer time is needed for Mg modified CaNbO₂N as V_{oc} was not completely restored after 1600 s, indicating that Mg modifications help to extend electron lifetime. More interestingly, after switching testing atmosphere from Ar to O₂, V_{oc} decay profile is much more accelerated in Mg modified CaNbO₂N than pristine one. As O₂ efficiently scavenges

electrons migrating to the surface, electron transportation from bulk to surface is expected to be easier after Mg modifications. This is consistent with previous speculations based on XRD analysis in which Nb-(O,N) bonds are strengthened in Mg modified CaNbO₂N, therefore, is favorable for charge migration. Furthermore, the photoluminescence (PL) emission spectra with light source excited at 420 nm were performed to evaluate the recombination of photoinduced carriers. As shown in Figure S8, Mg modified CaNbO₂N has lower PL intensity compared with pristine sample, indicating lower recombination rate of electrons and holes after Mg incorporating.

3.7. Band edge positions

The band edge positions of CaNbO₂N and Mg modified one were then determined by Mott-Schottky (MS) analysis and XPS valence band scan. Fig. 10a illustrates MS plot of both samples. Their flat band potential (V_{fb}) can be determined by extrapolating linear part of the curves down to energy axis according to MS equation: [78]

$$\frac{1}{C^2} = \frac{2}{\epsilon\epsilon_0 A^2 e N_D} \left(V - V_{fb} - \frac{k_B T}{e} \right)$$

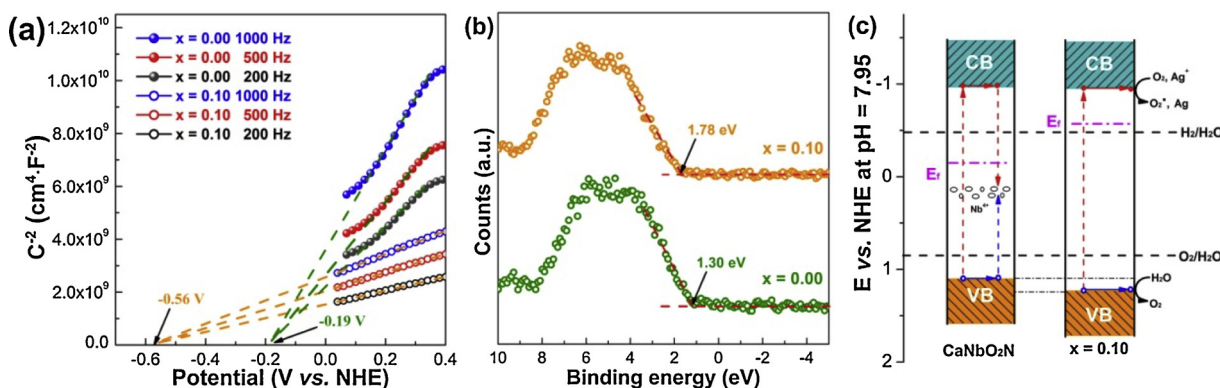


Fig. 10. (a) Mott-Schottky plots of pristine and Mg-modified CaNbO_2N under a fixed frequency of 200 Hz, 500 Hz and 1000 Hz at amplitude of 10 mV, (b) XPS valence band spectra, and (c) illustration of band edge positions of pristine and Mg-modified CaNbO_2N . Photoexcited electrons and holes are represented as filled and open circles.

where C is capacitance at the interface, A is electrode surface area, V is applied bias, T is absolute temperature, k_B is Boltzmann's constant, ϵ is the dielectric constant, N_D is the donor concentration. It can be seen from the plot that V_{fb} (i.e. Fermi level) of pristine CaNbO_2N is shifted negatively from -0.19 V to -0.56 V (vs NHE) after Mg modifications. XPS valence band scan suggests that energy gaps between the V_{fb} and the valence band maximum (VBM) are ~ 1.30 and ~ 1.78 eV before and after introducing Mg. Based on flat band potentials and XPS valence band scan, the valence band positions of CaNbO_2N before and after Mg modifications can be determined accordingly. On the other hand, the conduction band positions can then be deduced combining the position of VBM and the band gaps to obtain the complete band edge positions. A schematic illustration of band structures is displayed in Fig. 10c. The slight positive shift of VBM after Mg modifications implies that driving force for water oxidation will be higher in Mg modified samples. The much lower position of Fermi level in pristine CaNbO_2N is probably due to the high concentration of Nb^{4+} species that pins the Fermi level. Band bending across the depletion layer will thus be greater in Mg modified CaNbO_2N when Fermi level of sample powders is equilibrated with water redox potential, being likely another reason for high photocatalytic activity. Thereby, the much improved performance after introducing Mg into B site of CaNbO_2N can be understood as lower level of Nb^{4+} defects, higher charge mobility and separation as well as stronger driving force for water oxidation reactions.

4. Conclusions

In this study, a series of Mg-modified CaNbO_2N , i.e. $\text{CaNb}_{1-x}\text{Mg}_x\text{O}_{2+y}\text{N}_{1-y}$ ($0 \leq x \leq 0.2$) were prepared via ammonolysis of metal oxide precursors made by polymerized-complex method. Introducing Mg into B site of CaNbO_2N has apparent effects on a number of important properties such as unit cell parameters, optical absorption, nitrogen content and defects concentration. More specifically, Mg modifications lead to shrinkage of CaNbO_2N unit cell, enlargement of band gap values and decrease of nitrogen content and defects level. More importantly, photocatalytic activity for water oxidation reactions were much improved after introducing Mg into CaNbO_2N . Apparent quantum efficiency as high as 3.4% at 420 ± 20 nm was achieved in $\text{CaNb}_{0.9}\text{Mg}_{0.1}\text{O}_{2+y}\text{N}_{1-y}$ ($x = 0.1$) which stands as the highest AQE reported on CaNbO_2N . Further PEC analysis suggests that Mg modifications help to suppress charge recombination events, facilitate charge migration and separation as well as extend electron lifetime. Band edge positions before and after Mg modifications were also determined. It is also found that Mg modified CaNbO_2N has a higher driving force for water oxidation reactions under light illumination. This simple strategy of Mg modification can be extended to other perovskite oxynitrides where reduction of low charge defects i.e. Ti^{3+} , Nb^{4+} and Ta^{4+} is

needed.

Acknowledgment

This study was financially supported by the National Natural Science Foundation of China (Grant Nos. 21401142) and 1000 plan. This work is also supported by the Science and Technology Commission of Shanghai Municipality (14DZ2261100) and the Fundamental Research Funds for the Central Universities.

Appendix A. Supplementary data

Supplementary material related to this article can be found, in the online version, at doi:<https://doi.org/10.1016/j.apcatb.2018.12.033>.

References

- [1] N.S. Lewis, D.G. Nocera, Proc. Natl. Acad. Sci. 103 (2006) 15729–15735.
- [2] M. Grätzel, Nature 414 (2001) 338.
- [3] A. Kudo, Y. Miseki, Chem. Soc. Rev. 38 (2009) 253–278.
- [4] X. Li, J.G. Yu, M. Jaroniec, Chem. Soc. Rev. 45 (2016) 2603–2636.
- [5] Z.G. Zou, J.H. Ye, K. Sayama, H. Arakawa, Nature 414 (2001) 625–627.
- [6] X. Chen, S.S. Mao, Chem. Rev. 107 (2007) 2891–2959.
- [7] X.X. Xu, C. Randorn, P. Efstratiou, J.T.S. Irvine, Nat. Mater. 11 (2012) 595–598.
- [8] W.D. Shi, S.Y. Song, H.J. Zhang, Chem. Soc. Rev. 42 (2013) 5714–5743.
- [9] H.X. Li, Z.F. Bian, J. Zhu, D.Q. Zhang, G.S. Li, Y.N. Huo, H. Li, Y.F. Lu, J. Am. Chem. Soc. 129 (2007) 8406–8407.
- [10] S. Linic, P. Christopher, D.B. Ingram, Nat. Mater. 10 (2011) 911–921.
- [11] H. Zhang, S. Ni, Y. Mi, X. Xu, J. Catal. 359 (2018) 112–121.
- [12] M.A. Fox, M.T. Dulay, Chem. Rev. 93 (1993) 341–357.
- [13] A. Fujishima, K. Honda, Nature 238 (1972) 37–38.
- [14] X.B. Chen, S.H. Shen, L.J. Guo, S.S. Mao, Chem. Rev. 110 (2010) 6503–6570.
- [15] T.A. Betley, Q. Wu, T. Van Voorhis, D.G. Nocera, Inorg. Chem. 47 (2008) 1849–1861.
- [16] Y.W. Wang, D.Z. Zhu, X.X. Xu, ACS Appl. Mater. Interfaces 8 (2016) 35407–35418.
- [17] P. Zhou, J.G. Yu, M. Jaroniec, Adv. Mater. 26 (2014) 4920–4935.
- [18] M.L. Lv, X.Q. Sun, S.H. Wei, C. Shen, Y.L. Mi, X.X. Xu, Acs Nano 11 (2017) 11441–11448.
- [19] Y. Masubuchi, F. Kawamura, T. Taniguchi, S. Kikkawa, J. Eur. Ceram. Soc. 35 (2015) 1191–1197.
- [20] M.R. Brophy, S.M. Pilgrim, W.A. Schulze, J. Am. Ceram. Soc. 94 (2011) 4263–4268.
- [21] S. Wei, X. Xu, Appl. Catal., B 228 (2018) 10–18.
- [22] Y. Mizuno, H. Wagata, K. Yubuta, N. Zettsu, S. Oishi, K. Teshima, Crystengcomm 15 (2013) 8133–8138.
- [23] W.P. Si, D. Pergolesi, F. Haydous, A. Fluri, A. Wokaun, T. Lippert, Phys. Chem. Chem. Phys. 19 (2017) 656–662.
- [24] J.Y. Feng, W.J. Luo, T. Fang, H. Lv, Z.Q. Wang, J. Gao, W.M. Liu, T. Yu, Z.S. Li, Z.G. Zou, Adv. Funct. Mater. 24 (2014) 3535–3542.
- [25] K. Ueda, H. Kato, M. Kobayashi, M. Hara, M. Kakihana, J. Mater. Chem. A 1 (2013) 3667–3674.
- [26] F. Oehler, S.G. Ebbinghaus, Solid State Sci. 54 (2016) 43–48.
- [27] F. Oehler, R. Naumann, R. Koferstein, D. Hesse, S.G. Ebbinghaus, Mater. Res. Bull. 73 (2016) 276–283.
- [28] F. Yoshitomi, K. Sekizawa, K. Maeda, O. Ishitani, ACS Appl. Mater. Interfaces 7 (2015) 13092–13097.
- [29] K. Maeda, Prog. Solid State Chem. 51 (2018) 52–62.
- [30] T. Oshima, T. Ichiba, K.S. Qin, K. Muraoka, J.J.M. Vequizo, K. Hibino, R. Kuriki,

- S. Yamashita, K. Hongo, T. Uchiyama, K. Fujii, D.L. Lu, R. Maezono, A. Yamakata, H. Kato, K. Kimoto, M. Yashima, Y. Uchimoto, M. Kakihana, O. Ishitani, H. Kageyama, K. Maeda, *Angew. Chem. Int. Ed.* 57 (2018) 8154–8158.
- [31] Z.H. Pan, T. Hisatomi, Q. Wang, S.S. Chen, M. Nakabayashi, N. Shibata, C.S. Pan, T. Takata, M. Katayama, T. Minegishi, A. Kudo, K. Domen, *Acs Catal.* 6 (2016) 7188–7196.
- [32] J.S. Xu, C.S. Pan, T. Takata, K. Domen, *Chem. Commun.* 51 (2015) 7191–7194.
- [33] M. Matsukawa, R. Ishikawa, T. Hisatomi, Y. Moriya, N. Shibata, J. Kubota, Y. Ikuhara, K. Domen, *Nano Lett.* 14 (2014) 1038–1041.
- [34] R. Sasaki, K. Maeda, Y. Kako, K. Domen, *Appl. Catal. B* 128 (2012) 72–76.
- [35] L. Clark, J. Oro-Sole, K.S. Knight, A. Fuertes, J.P. Attfield, *Chem. Mater.* 25 (2013) 5004–5011.
- [36] H. Kato, K. Ueda, M. Kobayashi, M. Kakihana, *J. Mater. Chem. A* 3 (2015) 11824–11829.
- [37] L. Zhang, Y. Song, J.Y. Feng, T. Fang, Y.J. Zhong, Z.S. Li, Z.G. Zou, *Int. J. Hydrogen Energy* 39 (2014) 7697–7704.
- [38] M. Ahmed, X.X. Guo, *Inorg. Chem. Front.* 3 (2016) 578–590.
- [39] Y.H. Xie, Y.W. Wang, Z.F. Chen, X.X. Xu, *Chemsuschem* 9 (2016) 1403–1412.
- [40] F.F. Wu, M.L. Lv, X.Q. Sun, Y.H. Xie, H.M. Chen, S. Ni, G. Liu, X.X. Xu, *Chemcatchem* 8 (2016) 615–623.
- [41] Y.M. Song, J.Q. Dai, H. Zhang, *Comp. Mater. Sci.* 127 (2017) 180–186.
- [42] G. Zhang, G. Liu, L.Z. Wang, J.T.S. Irvine, *Chem. Soc. Rev.* 45 (2016) 5951–5984.
- [43] C. Chen, R.Z. Chen, L.Z. Wang, G. Liu, H.M. Cheng, *J. Mater. Chem. A* 4 (2016) 2783–2800.
- [44] K. Maeda, M. Higashi, B. Siritanaratkul, R. Abe, K. Domen, *J. Am. Chem. Soc.* 133 (2011) 12334–12337.
- [45] C. Izawa, T. Kobayashi, K. Kishida, T. Watanabe, *Adv. Mater. Sci. Eng.* (2014).
- [46] N. Kumar, A. Sundaresan, C.N.R. Rao, *Mater. Res. Bull.* 46 (2011) 2021–2024.
- [47] S.K. Sun, Y. Masubuchi, T. Motohashi, S. Kikkawa, *J. Eur. Ceram. Soc.* 35 (2015) 3289–3294.
- [48] X. Sun, G. Liu, X. Xu, *J. Mater. Chem. A* 6 (2018) 10947–10957.
- [49] F. Wu, G. Liu, X. Xu, *J. Catal.* 346 (2017) 10–20.
- [50] S. Wei, G. Zhang, X. Xu, *Appl. Catal. B* 237 (2018) 373–381.
- [51] C.S. Pan, T. Takata, M. Nakabayashi, T. Matsumoto, N. Shibata, Y. Ikuhara, K. Domen, *Angew. Chem. Int. Ed.* 54 (2015) 2955–2959.
- [52] F.F. Wu, X.Q. Sun, G. Liu, X.X. Xu, *Catal. Sci. Technol.* 7 (2017) 4640–4647.
- [53] G. Hitoki, T. Takata, J.N. Kondo, M. Hara, H. Kobayashi, K. Domen, *Electrochemistry* 70 (2002) 463–465.
- [54] B. Siritanaratkul, K. Maeda, T. Hisatomi, K. Domen, *Chemsuschem* 4 (2011) 74–78.
- [55] A. Larson, R. Von Dreele, *General Structure Analysis System (GSAS). Report LA-UR-86-748*, Los Alamos National Laboratory, Los Alamos, NM, 1987.
- [56] D. Zhu, Y. Wang, W. Lu, H. Zhang, Z. Song, D. Luo, L. Gan, M. Liu, D. Sun, *Carbon* 111 (2017) 667–674.
- [57] S.S. Chen, S. Shen, G.J. Liu, Y. Qi, F.X. Zhang, C. Li, *Angew. Chem. Int. Ed.* 54 (2015) 3047–3051.
- [58] D. Eisenberg, H.S. Ahn, A.J. Bard, *J. Am. Chem. Soc.* 136 (2014) 14011–14014.
- [59] M.J. Liao, J.Y. Feng, W.J. Luo, Z.Q. Wang, J.Y. Zhang, Z.S. Li, T. Yu, Z.G. Zou, *Adv. Funct. Mater.* 22 (2012) 3066–3074.
- [60] Y.-I. Kim, P.M. Woodward, K.Z. Baba-Kishi, C.W. Tai, *Chem. Mater.* 16 (2004) 1267–1276.
- [61] X.Q. Sun, Y. Mi, F. Jiao, X. Xu, *Acs Catal.* 8 (2018) 3209–3221.
- [62] A. Rachel, S.G. Ebbinghaus, M. Gungerich, P.J. Klar, J. Hanss, A. Weidenkaff, A. Reller, *Thermochim. Acta* 438 (2005) 134–143.
- [63] C.T. Chia, Y.C. Chen, H.F. Cheng, I.N. Lin, *J. Appl. Phys.* 94 (2003) 3360–3364.
- [64] S. Balaz, S.H. Porter, P.M. Woodward, L.J. Brinson, *Chem. Mater.* 25 (2013) 3337–3343.
- [65] G. King, P.M. Woodward, *J. Mater. Chem.* 20 (2010) 5785–5796.
- [66] J. Grins, P.O. Kall, G. Svensson, *J. Mater. Chem.* 4 (1994) 1293–1301.
- [67] D. Li, W.J. Li, C. Fasel, J. Shen, R. Riedel, *J. Alloys Compd.* 586 (2014) 567–573.
- [68] R. Aguiar, D. Logvinovich, A. Weidenkaff, A. Reller, S.G. Ebbinghaus, *Thermochim. Acta* 471 (2008) 55–60.
- [69] K. Isawa, R. Itti, J. Sugiyama, N. Koshizuka, H. Yamauchi, *Phys. Rev. B* 49 (1994) 3534–3538.
- [70] A. Darlinski, J. Halbritter, *Surf. Interface Anal.* 10 (1987) 223–237.
- [71] K. Kawashima, M. Hojaberdiiev, O. Mabayaje, B.R. Wygant, K. Yubuta, C.B. Mullins, K. Domen, K. Teshima, *Crystengcomm* 19 (2017) 5532–5541.
- [72] X.Q. Sun, Y.H. Xie, F.F. Wu, H.M. Chen, M.L. Lv, S. Ni, G. Liu, X.X. Xu, *Inorg. Chem.* 54 (2015) 7445–7453.
- [73] E. Nurlaela, S. Ould-Chikh, I. Llorens, J.L. Hazemann, K. Takanabe, *Chem. Mater.* 27 (2015) 5685–5694.
- [74] K. Maeda, K. Domen, *Angew. Chem., Int. Ed.* 51 (2012) 9865–9869.
- [75] D. Yamasita, T. Takata, M. Hara, J.N. Kondo, K. Domen, *Solid State Ionics* 172 (2004) 591–595.
- [76] B.H. Meekins, P.V. Kamat, *Acs Nano* 3 (2009) 3437–3446.
- [77] A. Zaban, M. Greenshtein, J. Bisquert, *Chemphyschem* 4 (2003) 859–864.
- [78] K. Gelderman, L. Lee, S.W. Donne, *J. Chem. Educ.* 84 (2007) 685–688.